# LANGMUIR

pubs.acs.org/Langmuir Article

# Ultrafast Synthesis of High Entropy Oxide Nanoparticles by Flame Spray Pyrolysis

Abhijit H. Phakatkar, Mahmoud Tamadoni Saray, Md Golam Rasul, Lioudmila V. Sorokina, Timothy G. Ritter, Tolou Shokuhfar,\* and Reza Shahbazian-Yassar\*



Cite This: Langmuir 2021, 37, 9059-9068

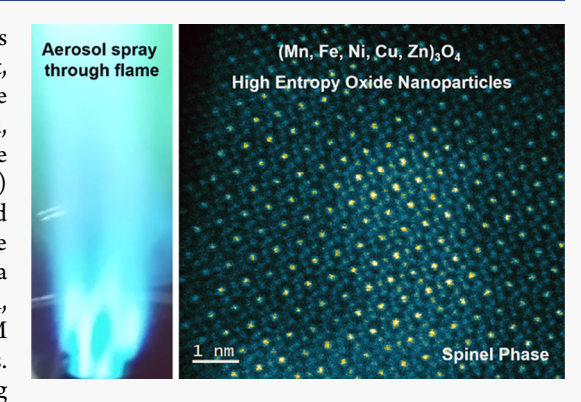


**ACCESS** 

Metrics & More

Article Recommendations

ABSTRACT: The synthesis of high entropy oxide (HEO) nanoparticles (NPs) possesses many challenges in terms of process complexity and cost, scalability, tailoring nanoparticle morphology, and rapid synthesis. Herein, we report the synthesis of novel single-phase solid solution (Mn, Fe, Ni, Cu, Zn)<sub>3</sub>(O)<sub>4</sub> quinary HEO NPs produced by a flame spray pyrolysis route. The aberration-corrected scanning transmission electron microscopy (STEM) technique is utilized to investigate the spinel crystal structure of synthesized HEO NPs, and energy-dispersive X-ray spectroscopy analysis confirmed the high entropy configuration of five metal elements in their oxide form within a single HEO nanoparticle. Selected area electron diffraction, X-ray diffraction, and Raman spectroscopy analysis results are in accordance with STEM results, providing the key attributes of a spinel crystal structure of HEO NPs. X-ray photoelectron spectroscopy results provide the insightful understanding



of chemical oxidation states of individual elements and their possible cation occupancy sites in the spinel-structured HEO NPs.

# ■ INTRODUCTION

Multicomponent metal nanoparticles (NPs) among the family of advanced nanocrystals are of vast interest in biomedical, catalysis,<sup>3,4</sup> and energy storage<sup>5,6</sup> fields. Recently, high entropy alloy (HEA) nanomaterials composed of five or more metals have attracted tremendous attention considering their unique and complex physicochemical properties derived from the high configurational entropy of mixing and tunable elemental compositional flexibility. Studies indicate that HEA nanomaterials possess superior properties including enhanced corrosion and wear resistance, thermal stability, superparamagnetic, and mechanical properties. 8-12 The increased configurational entropy is proposed to be the main factor contributing to the stability of solid solution in HEA. 13,14 The metal oxide NPs composed of multiple principal elements are equally being explored as multifunctional alternatives for antimicrobial, water purification, and catalytic applications. 13,15,16

The well-established methods to synthesize phase-separated and well-mixed alloyed multicomponent metal NPs include microemulsion approach, <sup>17</sup> microwave assisted approach, <sup>18</sup> wet chemical synthesis approach, <sup>19</sup> and microfluidic approach. <sup>20</sup> Considering the slow reaction kinetics constraining rapid heating and cooling rates, these techniques exhibit limitations for synthesizing multielement metallic NPs exceeding alloy composition more than three elements. Yao et al. <sup>21</sup> showed a novel carbothermal shock approach capable of

synthesizing HEA metal NPs composed of more than five traditionally immiscible elements by achieving rapid heating and cooling rates. Although this work is considered to be the pioneering work, the process is limited to only electrically conductive substrates and hence limiting the yield of NPs. To overcome the challenge of obtaining the high yield, Gao et al.7 showed a fast moving bed pyrolysis approach to synthesize denary HEA NPs on graphene oxide support and reliability to produce octonary HEA NPs. This synthesis method requires specialized equipment to achieve the rapid heating and cooling rates which can certainly lead to the high yield of HEA NPs. Recently, Yang et al.<sup>22</sup> showed the aerosol droplet-mediated approach assisted by the rapid tube furnace heating and quenching to achieve the scalable synthesis of HEA NPs. To minimize the initial investment cost for the setup and to obtain scalability for the probable industrial applications, herein we demonstrate the applicability of the aerosol-mediated flame spray pyrolysis (FSP) method to synthesize the single-phase solid solution complex high entropy oxide (HEO) NPs in the ambient environmental conditions.

 Received:
 April 22, 2021

 Revised:
 July 5, 2021

 Published:
 July 19, 2021





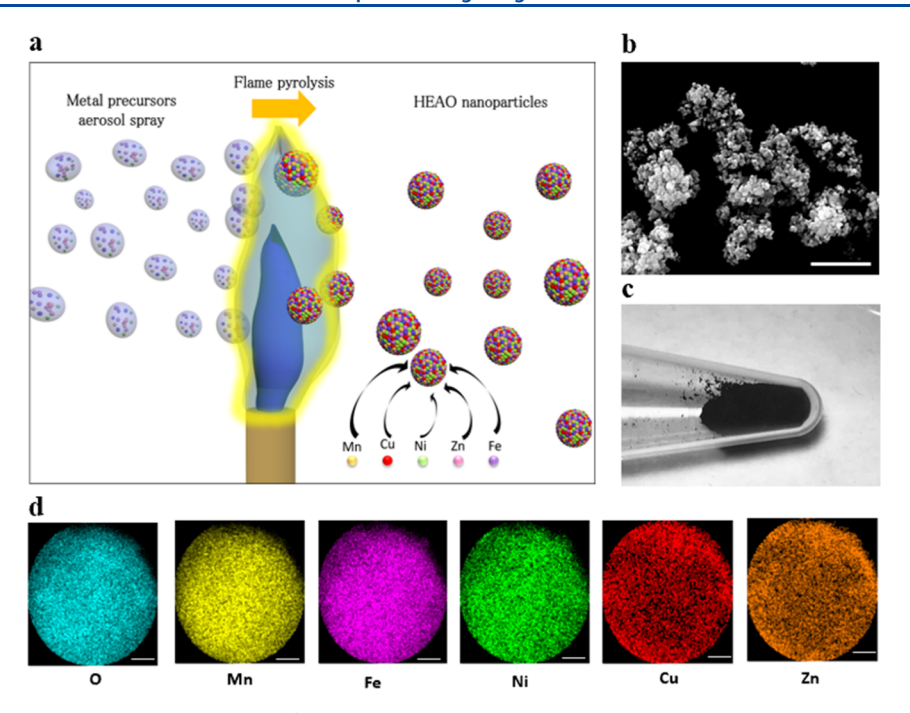


Figure 1. HEO NPs synthesis by the FSP technique. (a) Schematic representation of HEO NPs synthesis by the FSP route. (b) SEM micrograph of the synthesized HEO NPs (scale bar represents 250 nm). (c) Digital photograph of as-synthesized ( $[Mn_{0.18}Fe_{0.16}Ni_{0.18}Cu_{0.28}Zn_{0.19}]_3[O]_4$ ) HEO NPs. (d) STEM-EDS mapping of single HEO nanoparticle (scale bar represents 10 nm).

FSP is a well-established single-step aerosol-assisted rapid technique to produce high yields of metal oxide NPs via rapid vaporization and condensation of metal salt liquid precursors in the high temperature flame. 23,24 Previously, the FSP method is utilized to synthesize MgAl<sub>2</sub>O<sub>4</sub> (spinel),<sup>25</sup> CuAl<sub>2</sub>/Cu-O (inverted perovskite), 26 Ni<sub>k</sub>Mn<sub>1-k</sub>O (rock salt), 27 and LiV<sub>3</sub>O<sub>8</sub> (monoclinic)<sup>28</sup> single-phase complex metal oxide alloys. In the case of synthesizing multicomponent complex metal oxide NPs by the FSP route, the homogeneous NPs can be produced by increasing the gaseous fuel content to optimize the combustion enthalpy density of the flame.<sup>29</sup> Punginsang et al.<sup>30</sup> showed the importance of bismuth tungstate (Bi<sub>2</sub>WO<sub>6</sub>) NPs synthesized by the FSP method that possess very high phase purity and higher specific surface area in comparison with the NPs synthesized by hydrothermal, co-precipitation, ultrasonic spray pyrolysis, and sol-gel methods. Especially, single-phase solid solution HEA NPs possess unique attributes in regard to the superior phase stability against electron irradiation at elevated temperatures.<sup>31</sup> The single phase solid solution complex metal oxides are of tremendous interest considering their superior electrocatalytic, electrical and ionic conductivity, mechanical and thermal stability, and electrochemical reactivity properties. 32-34 Owing to the higher structural stability and elemental composition-dependent intrinsic and extrinsic properties of single phase HEO NPs, their facile and efficient synthesis is of greater importance for the various industrial applications.

In the present work, we synthesize the novel single-phase solid solution quinary HEO NPs composed of conventionally immiscible copper (Cu), manganese (Mn), iron (Fe), nickel (Ni), and zinc (Zn) elements in their oxide forms by using the FSP method. Briefly, the HEO NPs are synthesized by ultrafast quenching of the aerosol droplets (consisting of metal salts precursors dissolved in the ethanol solvent) directed through the high temperature (~1900 °C) flame zone. The synthesized (Mn, Fe, Ni, Cu, Zn)<sub>3</sub>O<sub>4</sub> NPs are systematically analyzed to investigate their microstructure and elemental composition by

using advanced transmission electron microscopy and conventional bulk characterization techniques. Additionally, chemical analysis of as-synthesized HEO NPs is performed by using an X-ray photoelectron spectroscopy (XPS) technique to obtain insights on oxidation state of individual elements integrated within high mixing entropy configuration. Results indicate that the synthesized (Mn, Fe, Ni, Cu, Zn) $_3$ O $_4$  NPs have a single-phase spinel crystal structure with high mixing entropy configuration.

# ■ RESULTS AND DISCUSSION

Figure 1 illustrates the key attributes of the HEO NPs synthesized by the FSP technique. The representative schematic ascribing to the overall synthesis theme of the present study can be observed in the Figure 1a. Figure 1b shows the low magnification scanning electron microscopy (SEM) micrograph of agglomerated HEO NPs, indicating the three-dimensional morphology of the synthesized NPs. The digital photograph (Figure 1c) of the as-synthesized (Mn, Fe, Ni, Cu, Zn)<sub>3</sub>(O)<sub>4</sub> HEO NPs indicates the potential of substrate-free bulk synthesis of HEO NPs, which shows their suitability for the various industrial applications. Figure 1d shows the elemental composition of single HEO NP synthesized by the FSP route, highlighting the miscibility of all five metal elements. Briefly, precursor solutions containing ethanol and metal chloride salt of each element were used for synthesizing HEO NPs. The equimolar concentration 0.01 M of metal chloride salts for iron, nickel, manganese, zinc, and copper elements was dissolved in an ethanol solvent to obtain the precursor solution. The crystal structure analysis and elemental composition evaluation of the as-synthesized HEO NPs are performed by using conventional bulk nanomaterial characterization and advanced scanning transmission electron microscopy (STEM) techniques.

Figure 2 illustrates the microstructural analysis of synthesized HEO NPs, which provides the valuable information of

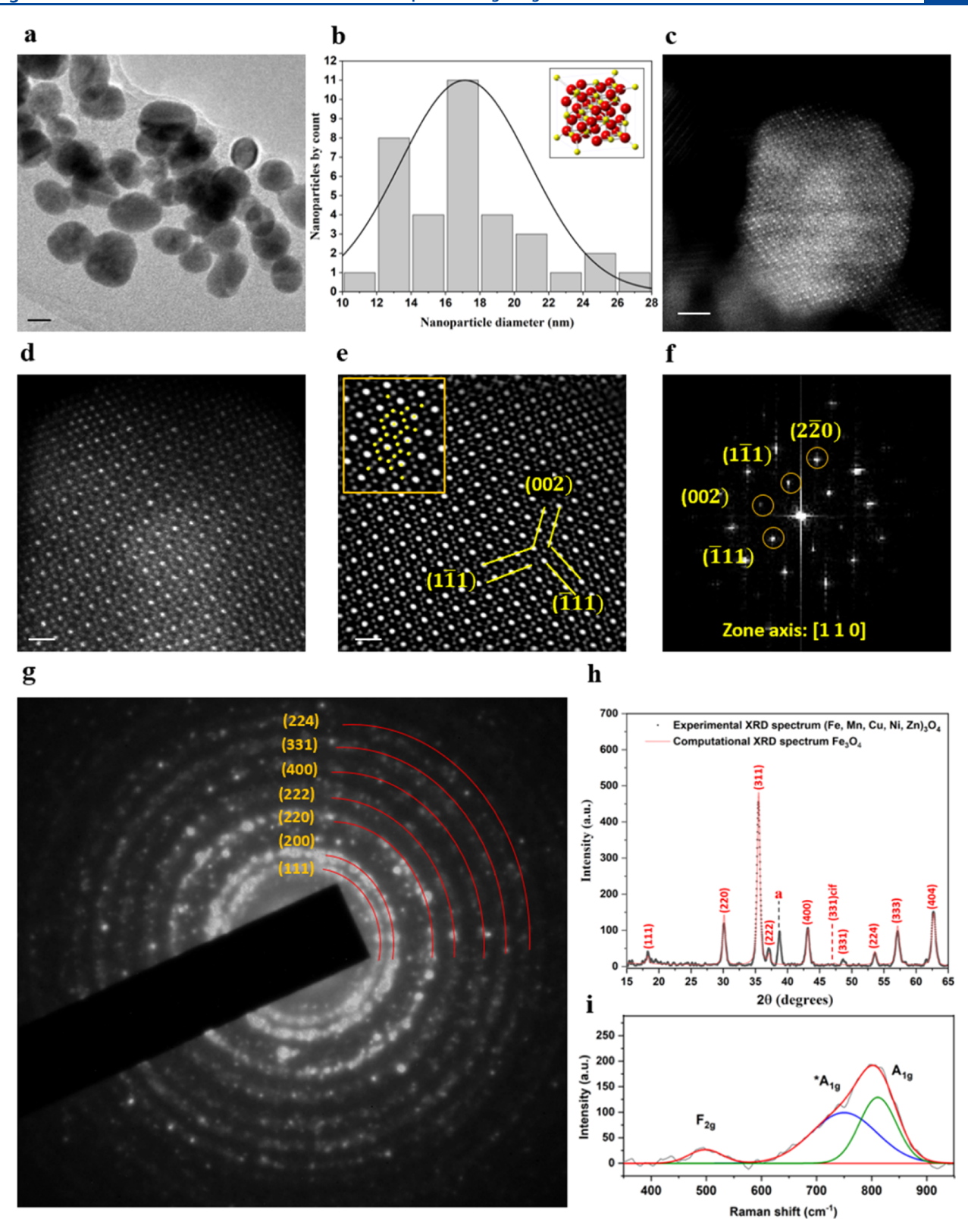
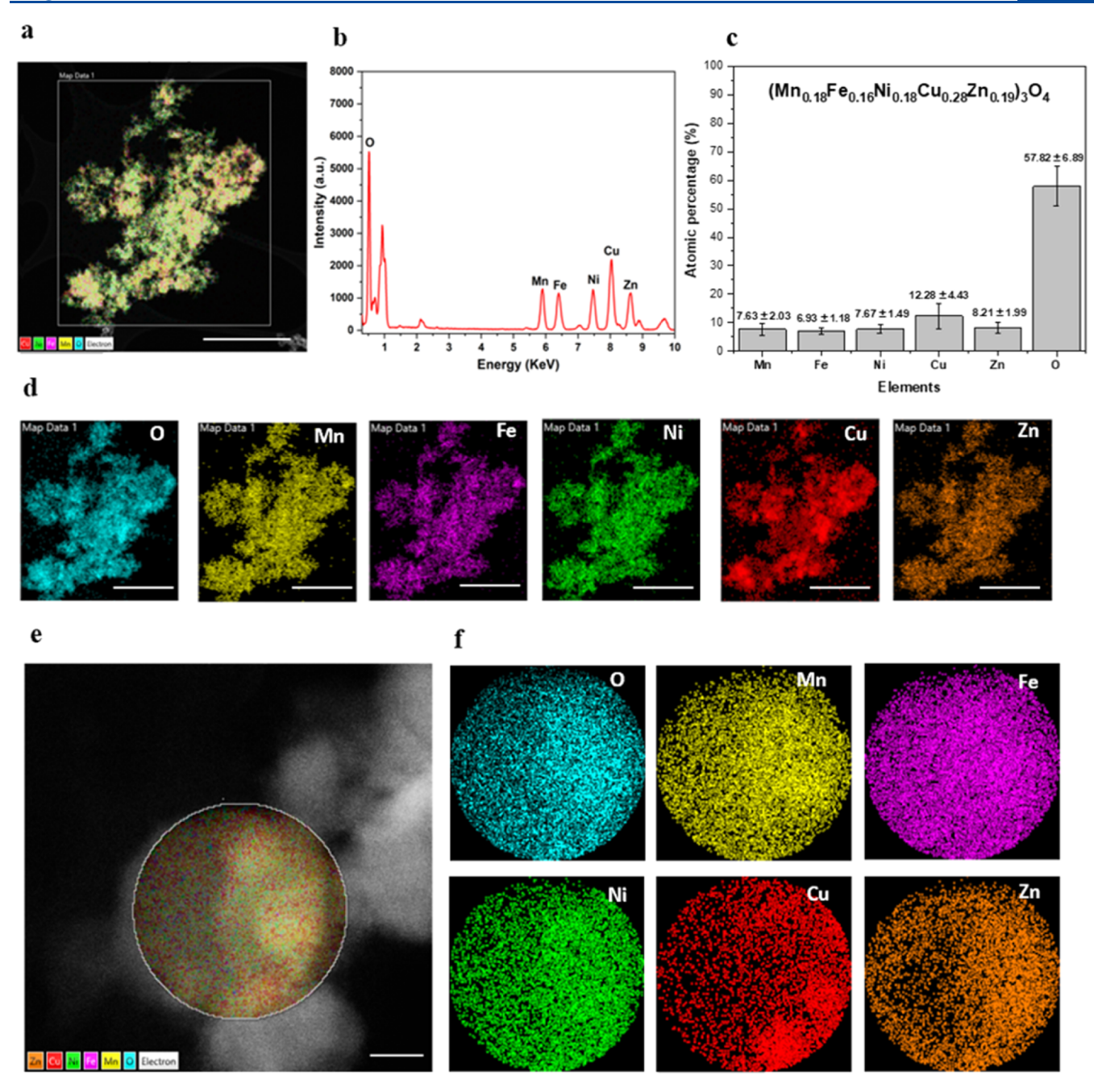


Figure 2. Crystal structure analysis of the synthesized HEO NPs. (a) Low-magnification TEM micrograph (scale bar represents 10 nm). (b) Statistical size distribution analysis of synthesized HEO NPs (mean average diameter of  $17.13 \pm 3.78$  nm). The inset represents the simulated spinel crystal structure, where red atoms represent oxygen sites and yellow atoms represent metal cations sites. (c) LAADF-STEM image of HEO NP (scale bar represents 2 nm). (d) Atomic resolution HAADF-STEM image of HEO NP (scale bar represents 1 nm). (e) IFFT image of HAADF-STEM image indicating the atomic planes and revealing the spinel crystal structure (scale bar represents 1 nm). The inset represents the simulated image with the best match to the magnified experimental image confirming the spinel crystal structure. (f) FFT analysis of HEO nanoparticle indicating lattice planes in the reciprocal space along the [110] zone axis. (g) SAED analysis of HEO NPs confirming the spinel crystal structure. (h) XRD pattern analysis of HEO NPs along with the Rietveld refinement confirming the spinel phase. (i) Raman spectroscopy analysis of HEO NPs indicating a deconvoluted Raman spectrum with the  $A_{1g}$ ,  $A_{1g}$ \*, and  $F_{2g}$  Raman active modes attributed to the spinel crystal structure.



**Figure 3.** STEM-EDS analysis of HEO NPs synthesized by the FSP technique. (a) Low-magnification EDS overlap mapping of HEO NPs (scalebar represents 500 nm). (b) EDS spectrum of HEO NPs corresponding to the low-magnification bulk region. (c) Elemental composition of HEO NPs calculated from the 15 different bulk regions attributed to the spinel crystal structure [Mn<sub>0.18</sub>Fe<sub>0.16</sub>Ni<sub>0.18</sub>Cu<sub>0.28</sub>Zn<sub>0.19</sub>]<sub>3</sub>O<sub>4</sub>. (d) EDS mapping of individual elements constituting HEO NPs in the bulk region. All scalebars represent 500 nm. (e) EDS mapping of single HEO nanoparticle (scalebar represents 5 nm). (f) EDS elemental mapping of all five individual elements present within the same quinary HEO nanoparticle indicating the high mixing entropy.

the complex crystal structure of multielement metal oxides. Figure 2a shows the low-magnification TEM micrograph of HEO NPs to gain understanding of the overall size distribution of the synthesized NPs. The statistical mean diameter distribution analysis of HEO NPs was calculated over 30 NPs as shown in Figure 2b, confirming the mean average diameter as 17.13 nm  $\pm$  3.78 nm. Figure 2c shows the low angle annular dark field (LAADF-STEM) image of HEO NP obtained at 12 Mx magnification indicating the presence of facets (002), (111) and (111) for the synthesized NPs. Figure 2d shows the atomic resolution HAADF-STEM image of the

same HEO NPs at 25 Mx magnification. Figure 2e shows a simulated inverse-fast Fourier transform (IFFT) HAADF-STEM image obtained from Figure 2d, where lattice plane directions can be clearly observed along the zone axis [110]. Additionally, the spinel metal oxide cubic crystal structure can be visualized. Figure 2f shows the fast Fourier transform (FFT) analysis. The FFT consists of bright diffraction spots rendering d-spacings of 4.132, 4.97, and 2.936 Å associated with three lattice planes (002), (111), and (220) respectively, suggesting that the HEO nanoparticle is compatible with spinel cubic metal oxide crystal structure with the presence of octahedral

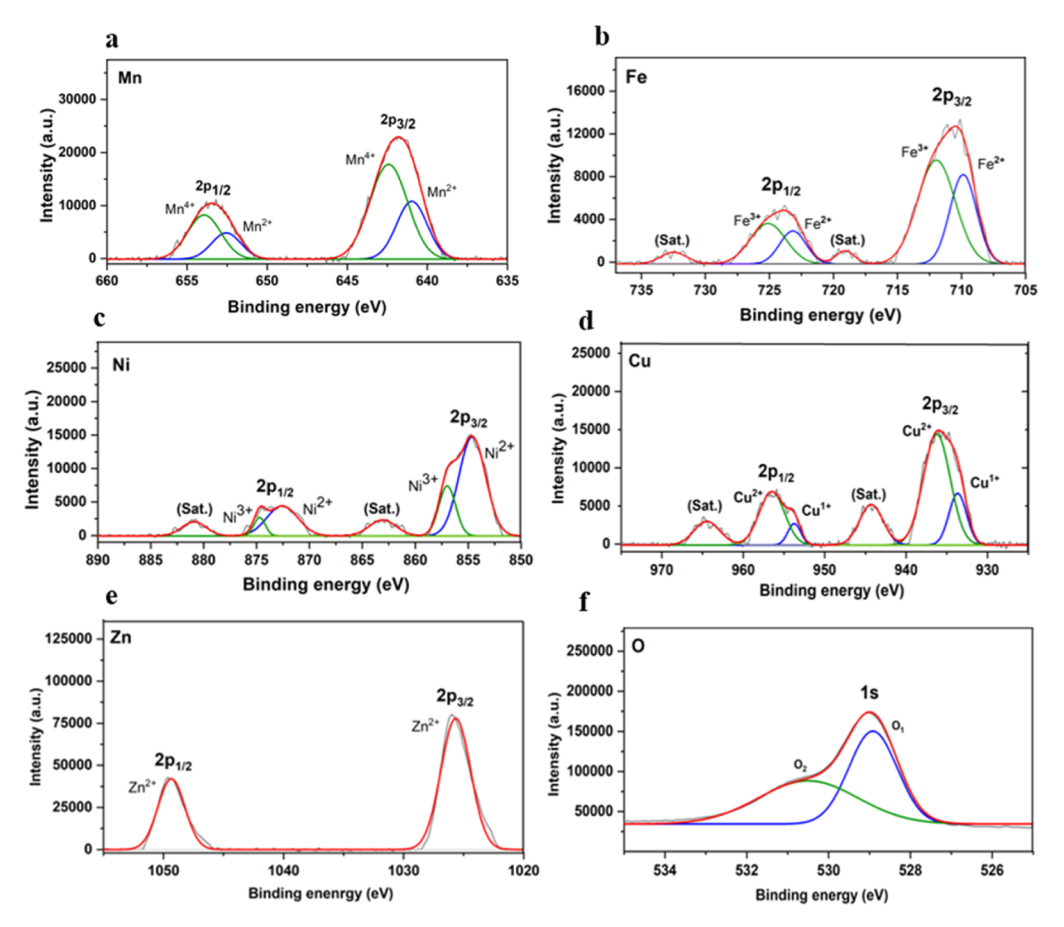


**Figure 4.** XPS analysis of HEO NPs. (a) Manganese 2p XPS spectrum of the HEO NPs confirming the presence of Mn<sup>2+</sup> and Mn<sup>4+</sup> oxidation states. (b) Iron 2p XPS spectrum of the HEO NPs confirming the presence of Fe<sup>2+</sup> and Fe<sup>3+</sup> oxidation states. (c) Nickel 2p XPS spectrum of the HEO NPs confirming the presence of Ni<sup>2+</sup> and Ni<sup>3+</sup> oxidation states. (d) Copper 2p XPS spectrum of the HEO NPs confirming the presence of Cu<sup>+</sup> and Cu<sup>2+</sup> oxidation states. (e) Zinc 2p XPS spectrum of the HEO NPs confirming the presence Zn<sup>2+</sup> oxidation states. (f) Oxygen 1 s XPS spectrum of the HEO NPs indicating presence of metal—oxygen bonding sites and defect sites in the spinel crystal structure.

and tetrahedral sites (lattice constant 8.39 Å). The corresponding parallel crystal planes can also be observed in the FFT diffraction pattern. To confirm the crystal structure from the large region of HEO NPs, a selected area electron diffraction (SAED) pattern is obtained as shown in Figure 2g. It can be observed that seven major diffraction rings indexed as (111), (200), (220), (222), (400), (331), and (224) lattice planes correspond to the spinel crystal structure.<sup>35</sup> The obtained X-ray diffraction (XRD) spectrum of HEO NPs (Figure 2h) supports the results of SAED pattern analysis. In total, nine peaks affiliated (111), (220), (113), (222), (400), (331), (224), (333), and (404) crystal lattice planes corresponding to the spinel cubic crystal structure can be observed in Figure 2h. 36 The experimental XRD spectrum qualitative analysis with the Rietveld refinement method clearly represents the perfect overlap of experimental and computational major (high intensity) characteristic peaks of the spinel phase. Results also indicate that there are two features in the XRD spectrum; one peak with a low intensity (331) plane and one additional XRD peak (labeled as "a") are offset from the computational standard spinel phase XRD spectrum. Studies indicate that for HEO or multielement NPs, the XRD peak intensities can be lower as compared to those of conventional monometallic NPs having the same crystal structure. The respective effect of reduced intensity of Bragg's diffraction is due to atoms deviating from the lattice sites attributed to their

variation in the atomic radii in the complex HEO NPs.<sup>37</sup> In the XRD spectrum of HEO NPs, the presence of asymmetric peaks can appear due to stacking defects or distribution of atoms of different elements at the lattice sites.<sup>38</sup> Additionally, as an effect of increasing principal elements in the HEO crystal structure, the XRD peak intensities decrease.<sup>39</sup> The size of NPs affects the XRD peak characteristics, as upon decreasing the NP size, the peaks possess a tendency to broaden.<sup>38</sup> The lattice distortion in HEO NPs can cause the positive or negative paradigm shift of XRD peaks.<sup>40</sup> In the obtained experimental XRD data (Figure 2h), for plane (331), the slight positive shift by  $1.35^{\circ}~2\theta$  diffraction angle is observed as compared with the standard Fe<sub>3</sub>O<sub>4</sub> computed XRD pattern. It indicates that the lattice distortion was induced in the synthesized HEO NPs. Also, in the experimental XRD pattern, one extra peak located at  $38.75^{\circ}$   $2\theta$  diffraction angle is observed, which is not a characteristic peak of the standard spinel crystal structure. The occurrence of an extra XRD peak in the case of HEO NPs is possibly due to the lattice distortion established by charge density accumulation. 41 Ślebarski et al. 42 with the help of density functional theory (DFT) calculations have proven that the generation of charge wave that occurred due to the loss and accumulation of spatial charge of individual elements in high entropy configuration results in the strong covalent bonding between specific elements and hence promotes the lattice distortion. The evidence of the single-phase solid solution

spinel crystal structure as obtained from the SAED pattern and XRD spectrum bulk quantity of nanomaterials analysis results is supplemented with the Raman spectroscopy measurements. Figure 2i shows the obtained Raman spectrum (350-950 cm<sup>-1</sup>) acquired from the HEO NPs indicating the Raman active modes  $A_{1g}$ ,  $A_{1g}^*$  and  $F_{2g}$ . The Raman fingerprints of a spinel crystal structure shows that the metal cations with +2 oxidation state (M2+) favorably occupy tetrahedral sites and those with the +3 oxidation state  $(M^{3+})$  are likely to occupy octahedral sites.  $^{44}~A_{\rm lg}$  characteristic Raman mode at the  $811.31\,$ cm<sup>-1</sup> wavenumber corresponds to the divalent metal cationoxygen (M2+-O) stretching vibration occupied at the tetrahedral site in the spinel crystal structure. 43 A\* Raman mode at the 750.09 cm<sup>-1</sup> wavenumber appears due to completely random cation occupancy at tetrahedral sites experiencing M<sup>2+</sup>-O stretching vibration, which confirms the disordered occupancy of different cations at tetrahedral and octahedral sites in the spinel crystal structure of synthesized (Mn, Fe, Ni, Cu,  $Zn)_3(O)_4$  HEO NPs.<sup>43</sup>  $A_{1g}$  mode occurrence at lower wavenumbers can be due to the presence of heavier cations in the spinel crystal structure. At the 498.74 cm<sup>-1</sup> wavenumber, the F<sub>2g</sub> Raman band appears, which can be associated with asymmetric stretching between the metal cation and oxygen bond at tetrahedral sites. 43 Raman spectroscopy results show the evidence of the disordered occupancy of multiple cations attributed to the configurational mixing entropy in the synthesized HEO NPs.

The elemental composition of synthesized HEO NPs is evaluated by using an energy-dispersive X-ray spectroscopy (EDS) technique. 22 Figure 3 shows the EDS analysis of synthesized HEO NPs obtained in the STEM mode. Figure 3a shows the low-magnification EDS mapping of synthesized HEO NPs and the corresponding EDS spectrum, confirming the presence of all five elements that can be observed in Figure 3b. Figure 3c represents elemental composition analysis averaged over the 15 large regions of synthesized HEO NPs, where atomic percentage of each individual element can be observed. The final elemental composition of the synthesized HEO NPs of  $(Mn_{0.18}Fe_{0.16}Ni_{0.18}Cu_{0.28}Zn_{0.19})_3O_4$  is evaluated from the atomic percentages of individual elements Mn (7.63  $\pm$  2.03)%, Fe (6.93  $\pm$  1.18)%, Ni (7.67  $\pm$  1.49)%, Cu (12.28  $\pm$  4.43)%, Zn (8.21  $\pm$  1.99)%, and O (57.82  $\pm$  6.89)%, which also comprehends the spinel crystal structure with the metal to oxygen ratio to be 3/4.45 The homogeneous distribution of individual elements in the synthesized HEO NPs can be observed over a large region in Figure 3d. Further, to confirm the well mixing entropy of elements within a single HEO nanoparticle, EDS mapping of a nanoparticle with a 18.4 nm diameter is performed (Figure 3e). The corresponding elemental distribution map for each element is shown in Figure 3f, which confirms the homogeneous and consistent presence of all (Mn, Fe, Ni, Cu, Zn, and O) elements within a single quinary HEO nanoparticle.

Figure 4 shows the qualitative XPS analysis of as-synthesized HEO NPs. High-resolution deconvoluted XPS spectra for individual elements present within HEO NPs are shown in Figure 4a–f. The fine scan 2p core-state XPS spectra of Mn and the corresponding deconvoluted oxidation peak intensities are shown in Figure 4a. For manganese,  $2p_{3/2}$  and  $2p_{1/2}$  core states that occurred due to spin orbit splitting are located at 641.75 and 653.42 eV, respectively, with an energy splitting of 11.67 eV, which is in accordance with the previously reported studies attributed to the Mn<sub>3</sub>O<sub>4</sub> spinel crystal structure. <sup>46</sup> The

Mn 2p<sub>3/2</sub> peak comprises two components with the binding energies of 640.96 and 642.41 eV, which are attributed to Mn<sup>24</sup> and Mn<sup>4+</sup> oxidation states. 47 The theoretical Mn<sub>3</sub>O<sub>4</sub> manganese oxide structure is composed of MnO2-2MnO with the ratio of Mn<sup>2+</sup>/Mn<sup>4+</sup> of 1:2. 46,47 The evaluated intensity ratio for Mn<sup>2+</sup>/Mn<sup>4+</sup> oxidation states deconvoluted from the  $2p_{3/2}$  peak is 1:2.034 which is in good agreement with the respective theoretical value. The presence of Mn<sup>2+</sup> and Mn<sup>4+</sup> oxidation states also indicates that manganese species in the synthesized HEO NPs spinel crystal structure can occupy both tetrahedral and octahedral sites. Figure 4b shows the 2p core-state XPS spectra of Fe as 2p<sub>3/2</sub> and 2p<sub>1/2</sub> located at 710.46 and 723.85 eV with an energy splitting of 13.39 eV. The deconvoluted  $2p_{3/2}$ ,  $2p_{1/2}$ , and satellite peaks confirm the presence of Fe<sup>2+</sup> and Fe<sup>3+</sup> oxidation states attributed to the Fe<sub>3</sub>O<sub>4</sub> (alternatively expressed as FeO·Fe<sub>2</sub>O<sub>3</sub>) phase.<sup>48</sup> Deconvoluted two 2p spectral bands appearing at 711.97 eV  $(2p_{3/2})$  and 725.11  $(2p_{1/2})$  eV are the characteristic peaks of Fe<sup>3+</sup> species, and those appearing at 709.86 eV  $(2p_{3/2})$  and 723.17 eV  $(2p_{1/2})$  belong to Fe<sup>2+</sup> species.<sup>48</sup> Additionally, satellite peaks occurring due to the ionization of atomic inner shells are located at 719.09 and 732.49 eV, which confirm the successful formation of the Fe<sub>3</sub>O<sub>4</sub> spinel phase.<sup>48</sup> In the synthesized HEO NPs, iron species can occupy both tetrahedral (favorably Fe<sup>2+</sup>) and octahedral (favorably Fe<sup>3+</sup>) crystal sites. 49 In Figure 4c, XPS spectra of Ni represent the 2p core energy states for Ni. As an effect of spin orbit, splitting  $2p_{3/2}$  and  $2p_{1/2}$  energy states appear at 854.66 and 872.56 eV, respectively, with an energy splitting of 17.9 eV. The satellite peaks appearing at 863.07 and 880.9 eV indicate the presence of mixed valence oxidation states of Ni. The deconvoluted spectra show the presence of the Ni<sup>2+</sup> oxidation state at 854.66 eV  $(2p_{3/2})$  and 872.56 eV  $(2p_{1/2})$  and that of the associated  $Ni^{3+}$  oxidation state at 856.98 eV  $(2p_{3/2})$  and 874.71 eV  $(2p_{1/2})^{50}$  Results indicate that nickel species can occupy both tetrahedral (favorably Ni<sup>2+</sup>) and octahedral (favorably Ni<sup>3+</sup>) crystal sites in the synthesized HEO NPs. The deconvolution of the 2p<sub>3/2</sub> core state into Ni<sup>2+</sup> and Ni<sup>3+</sup> species and their respective intensity ratio of 3.14/1 for Ni<sup>2+</sup>/Ni<sup>3+</sup> indicate that the dominance of the Ni<sup>2+</sup> oxidation state existence occupying mainly tetrahedral sites in the spinel phase. The XPS fine spectra of the Cu 2p energy state are shown in Figure 4d. Due to the split spinning orbital, the Cu 2p<sub>3/2</sub> band center appears at 935.60 eV and the Cu  $2p_{1/2}$  band center appears at 956.14 eV, where splitting energy difference is 20.54 eV.51 The deconvoluted XPS Cu 2p spectra show the presence of the Cu<sup>2+</sup> oxidation state at 936.24 eV for 2p<sub>3/2</sub> and at 956.48 eV for 2p<sub>1/2</sub>. Moreover, the presence of the Cu<sup>+</sup> oxidation state can be confirmed with deconvoluted XPS spectra band centers at 933.66 eV for  $2p_{3/2}$  and 953.74 eV for  $2p_{1/2}$ . It needs to be highlighted that the presence of a shakeup satellite peak at 944.28 eV confirms the presence of a dominant Cu<sup>2+</sup> oxidation state, occupying mainly tetrahedral sites in the synthesized HEO NPs spinel crystal structure. 50 Further, the dominant presence of the Cu<sup>2+</sup> oxidation state over the Cu<sup>1</sup> oxidation state can also be evaluated from the deconvoluted intensity ratio to be 3.29:1 at the  $2p_{3/2}$  energy state. The XPS 2p spectra of Zn integrated within HEO NPs is shown in Figure 4e, where Zn  $2p_{3/2}$  and  $2p_{1/2}$  core energy states are located at 1025.66 and 1049.34 eV, respectively, with the binding energy difference of 23.68 eV. The separation of  $2p_{3/2}$  and  $2p_{1/2}$  peaks ~23 eV is attributed to the characteristic  $Zn^{2+}$  species. In the synthesized HEO NPs, it is indicated that all the Zn

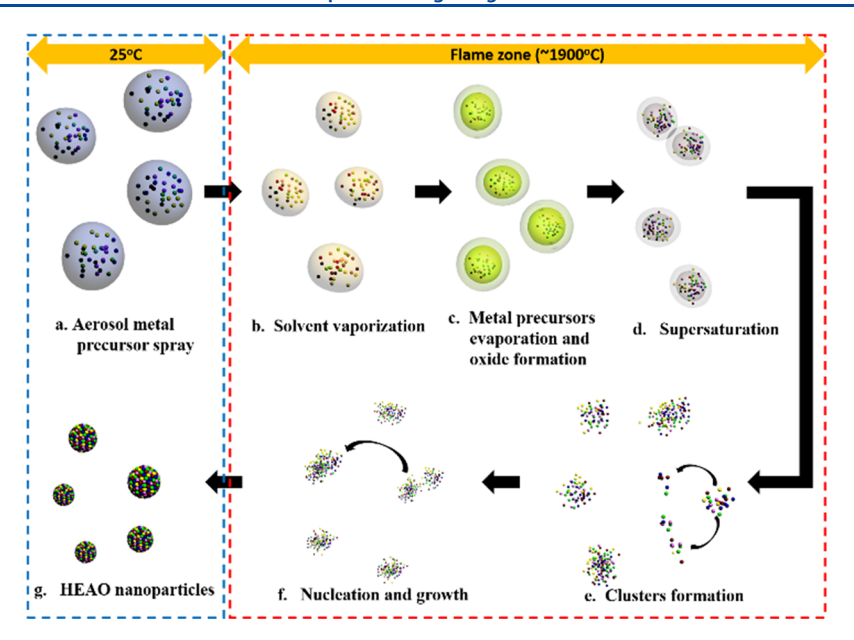


Figure 5. Proposed mechanism for the formation of HEO NPs via the FSP route.

species (with the +2 oxidation state) can occupy dominantly tetrahedral sites in the spinel crystal structure. Figure 4f shows the O 1 s orbital characteristic features. The oxygen 1 s peak located at 529 eV binding energy is deconvoluted systematically, and the corresponding O1 and O2 two peaks are indicated at 528.92 and 530.57 eV, respectively. The deconvoluted intense peak at 528.92 eV represents respective oxygen-metal bonds, and the deconvoluted lower intensity peak at 530.57 eV represents the defect sites with a low-oxygen coordination number within synthesized HEO NPs. 50 Even though XPS is a very well-known method to evaluate the oxidation states of individual elements composed within multimetallic and HEA nanostructures, there exist handful of reports which focus on the chemical shifts occurring during the XPS characterization.<sup>53</sup> It is important to note that in the quinary HEO NPs, few metal species can act as electron acceptors, causing negative chemical shift from the characteristic binding energy, while the remaining metal species can behave as electron donors, causing a positive chemical shift.

The molar configurational entropy for the metal oxide alloys can be calculated by using the equation 54,55

$$S_{\text{configuration}} = -R \left[ \left( \sum_{i=1}^{N} x_i \ln x_i \right)_{\text{cation-site}} + \left( \sum_{j=1}^{N} x_j \ln x_j \right)_{\text{anion-site}} \right]$$

where  $x_i$  and  $x_j$  represent the mole fraction of elements present in the cation and anion sites, respectively, and R represents the universal gas constant. The synthesized metal oxide alloy  $[(Mn,Fe,Ni,Cu,Zn)_3O_4$  spinel structure] configures the mixing entropy of 1.57 R confirming the HEA category, attributed to its calculated theoretical value as >1.50 R.<sup>54</sup> The atomic size polydispersity  $(\delta)$  is an accepted indicator to be  $\delta < 6$  to confirm the presence of a single phase solid solution in the HEA configuration.<sup>56</sup> The synthesized HEO NPs display the characteristics of single phase solid solution with the  $\delta$  value as

4.55, which is in accordance with the obtained microstructural and elemental analysis of synthesized HEO NPs.

The FSP process comprises the interplay between the local high flame temperature and large temperature gradient along the flame axis. In this process, the local high temperature promotes the formation of highly crystalline and homogeneous NPs and their growth by sintering and coalescence events. The large temperature gradients and short resident times (in milliseconds) maintain the nanoscale characteristics of the particles. 57,58 The possible stages of HEO NP formation via an FSP route are depicted in Figure 5. Briefly, the gaseous phase to particle generation mechanism is considered. 59 The aerosol spray-containing microdroplets of the metal salt precursor present in an ethanol solvent were generated with the spray nozzle at room temperature under atmospheric environmental conditions. Upon entering the flame zone, instantaneous solvent vaporization and metal precursor evaporation could take place during the initial stage of pyrolysis. \$59,60 Vaporized metal can instantaneously react with the oxygen available in the environment to form the respective gaseous metal oxides. 61,62 The corresponding gas phase metal precursor to oxide formation chemical reactions can be represented as

$$M-Cl_{(g)} \to M_{(g)} + Cl_{2(g)}$$
 (1)

$$M_{(g)} + O_{2(g)} \rightarrow M - O_{(g)}$$
 (2)

In the case of HEO NPs, a multiple metal salt precursor can possibly vaporize simultaneously into the gaseous phase by considering the FSP setup flame temperature (~1900 °C). Evaporation of solvent can cause supersaturation of gaseous phase metal oxides within the microdroplet. The metal oxide vapor species can lead to the nucleation of solid metal oxide NPs.<sup>63</sup> The intermediate steps are likely to include the formation of clusters considering the homogeneous nucleation. The clusters which can form nanosized particles can continue to grow by coagulation and sintering.<sup>58,64</sup> As the synthesized HEO NPs were dense and crystalline, the solvent evaporation rate was more likely to be slower than the solute diffusion rate during the formation process.<sup>65</sup>

#### CONCLUSIONS

In summary, we synthesized novel (Mn, Fe, Ni, Cu, Zn)<sub>3</sub>O<sub>4</sub> HEO NPs by the FSP method. STEM analysis shows that the synthesized HEO NPs are single phase solid solution spinelstructured with the lattice constant of 8.39 Å. SAED and XRD characterization results are in good agreement with STEM atomic resolution results, which confirms the microstructure of HEO NPs over the bulk region to be spinel-structured. XRD results also indicate the presence of lattice distortions in the synthesized HEO NPs. Raman spectroscopy modes A<sub>1g</sub>, F<sub>2g</sub>, and A<sub>1g</sub> corresponding to divalent metal cation—oxygen (M<sup>2+</sup>— O) stretching vibrations indicate the evidence of spinel crystal structure fingerprints. EDS results provide the evidence of a high entropy configuration of five metal elements in their oxide form within a single HEO NP. XPS analysis of HEO NPs shows the 2p spin orbital splitting  $(2p_{3/2})$  and  $(2p_{1/2})$ characteristics of each element. XPS results confirm that the oxidation states for the each of five elements varies, considering their respective coordination with oxygen elements or possibly with the neighboring metal cations. Moreover, XPS results provide key insights of individual metal cation occupancy at the tetrahedral and octahedral sites in the spinel-structured HEO NPs.

#### MATERIALS AND METHODS

**Synthesis.** HEO NPs were synthesized by a one-step and ultrafast aerosol-mediated FSP technique. Manganese chloride tetrahydrate (MnCl<sub>2</sub>·4H<sub>2</sub>O, Fisher Scientific), iron(III) chloride (FeCl<sub>3</sub>, Sigma-Aldrich), nickel(II) chloride hexahydrate (NiCl2·6H2O, Sigma-Aldrich), copper(II) chloride dihydrate (CuCl<sub>2</sub>·2H<sub>2</sub>O, Sigma-Aldrich), and zinc chloride (ZnCl2, Sigma-Aldrich) were utilized as received for preparing the metal salt precursor solution. Absolute ethanol (200 Proof, Fisher Scientific) was used as the solvent. Ethanol, also being an economical choice, can homogeneously dissolve hydrated metal chloride salt precursors due to its polar hydroxyl end present in its chemical chain. Metal salt precursor solution was prepared by dissolving equimolar (0.01 M) metal salt concentrations of manganese, iron, nickel, copper, and zinc elements in the ethanol solution. To achieve the homogeneously mixed precursor solution, the solution was continuously stirred for 3 h at 700 rpm, and successive 20 min of ultrasonication was used. The twinfluid nozzle (0.5 mm internal diameter) with air-assisted external mixing capability was utilized to generate the aerosol droplets. The compressed air was used as the atomizing gas. The precursor solution flow rate was 5 mL/min. The precursor solution aerosol droplets were directed through the propane torch flame (~1900 °C). The flame conditions were kept consistent throughout the synthesis process. The flow rate for propane fuel gas was 4.2 L/min, and the (air/propane gas) ratio was maintained (24/1). The synthesized HEO NPs from the flame were collected in the liquid bath via a quartz tube connected with the vacuum pump. The obtained yield of HEO NPs with the consideration of system losses was about 68%.

**Characterization.** SEM analysis was performed to assess the three-dimensional morphology of synthesized HEO NPs. For SEM analysis, a Hitachi S-3000N microscope was used. The synthesized HEO NPs dispersed in *iso*-propyl alcohol sample were drop-cast on a silicon wafer. The operating parameters of an accelerating voltage of 8.0 kV and working distance of 5.5 mm were utilized to obtain the SEM micrographs.

To evaluate the mean average diameter of synthesized HEO NPs, low magnification TEM analysis was performed. A JEOL JEM-3010 transmission electron microscope operated at 300 keV was utilized to obtain low-magnification TEM micrographs. SAED analysis of HEO NPs is performed with the same microscope by using the TEM diffraction mode. The camera length of 20 cm was utilized.

HEO NPs Raman spectroscopy analysis was performed on a Renishaw inVia Reflex with a green 532 nm laser with a 20 s exposure time with 3 times accumulation. A long distance optical objective lens (50×) was used to acquire Raman spectra within the range 200–1000  $\rm cm^{-1}$ .

The XRD analysis of HEO NPs was performed by using a Bruker nano-Discover 8 instrument. The XRD scan was acquired in the 15 and 65° range of  $2\theta$  diffraction angles with 2025 W power, 1 s time step, and at  $0.02\theta$  resolution. To confirm the presence of single-phase solid solution spinel phase in the XRD spectrum, the standard magnetite (Fe<sub>3</sub>O<sub>4</sub>) spinel crystal structure CIF file (1011032) with a Fd3m space group was utilized to perform the Rietveld refinement method. The Rietveld refinement was performed by using "Material Analysis Using Diffraction" (MAUD) software.

To analyze the crystal structure of the synthesized HEO NP, aberration-corrected JEOL ARM200CF TEM with a cold field emission gun operated at 200 kV and with a 22 mrad convergence angle was utilized in the STEM mode. High-angle annular dark field (HAADF) images were acquired with an Orius CCD camera with 512 × 512 scanning resolution.

To perform the quantitative elemental analysis of the synthesized HEO NPs, STEM-EDS was performed by using aberration-corrected JEOL ARM200CF TEM. The elemental spectra were obtained and mapping was carried out by using the Oxford EDS system by utilizing the drift corrector and the acquisition time of 7.5 min.

The qualitative chemical analysis of HEO NPs was performed with the help of XPS characterization. XPS analysis was performed using a Thermo Scientific ESCALAB 250Xi instrument. The source gun type Al K-alpha at 500  $\mu$ m spot size in the standard mode was utilized to acquire XPS spectra for individual (Mn, Fe, Ni, Cu, Zn, O) elements with 0.1 eV energy step resolution.

# AUTHOR INFORMATION

#### **Corresponding Authors**

Tolou Shokuhfar — Department of Bioengineering, University of Illinois at Chicago, Chicago, Illinois 60607, United States; Email: tolou@uic.edu

Reza Shahbazian-Yassar — Department of Mechanical and Industrial Engineering, University of Illinois at Chicago, Chicago, Illinois 60607, United States; oorcid.org/0000-0002-7744-4780; Email: rsyassar@uic.edu

# Authors

Abhijit H. Phakatkar – Department of Bioengineering, University of Illinois at Chicago, Chicago, Illinois 60607, United States

Mahmoud Tamadoni Saray — Department of Mechanical and Industrial Engineering, University of Illinois at Chicago, Chicago, Illinois 60607, United States

Md Golam Rasul — Department of Mechanical and Industrial Engineering, University of Illinois at Chicago, Chicago, Illinois 60607, United States

Lioudmila V. Sorokina — Civil and Materials Engineering, University of Illinois at Chicago, Chicago, Illinois 60607, United States

Timothy G. Ritter — Civil and Materials Engineering, University of Illinois at Chicago, Chicago, Illinois 60607, United States; Occid.org/0000-0002-5139-1908

Complete contact information is available at: https://pubs.acs.org/10.1021/acs.langmuir.1c01105

# **Author Contributions**

A.H.P. and M.T.S. performed the HEO NP synthesis experiments. A.H.P. performed the TEM and STEM imaging and SAED and STEM-EDS characterization. A.H.P. wrote the manuscript. M.G.R. performed XPS characterization of HEO NPs. L.V.S. worked on Raman analysis of HEO NPs. T.G.R. performed XRD characterization of HEO NPs. R.S.Y. and T.S.

conceptualized and supervised the project. All authors proofread, commented on, and approved the final manuscript for submission.

#### **Notes**

The authors declare no competing financial interest.

# ACKNOWLEDGMENTS

The present work made use of instruments in the Electron Microscopy Core of Research Resources Centre at University of Illinois at Chicago. Prof. R. Shahbazian-Yassar is thankful to National Science Foundation (NSF) for award number DMR-1809439. Prof. Shokuhfar acknowledges the financial support from NSF award number DMR-1710049.

# ABBREVIATIONS

HEO, high entropy oxide; NPs, nanoparticles; HEA, high entropy alloy; STEM, scanning transmission electron microscopy; FSP, flame spray pyrolysis; TEM, transmission electron microscopy; SEM, scanning electron microscopy; HAADF, high angle annular dark field; SAED, selected area electron diffraction; FFT, fast Fourier transform; IFFT, inverse-fast Fourier transform; XRD, X-ray diffraction; EDS, energy dispersive X-ray spectroscopy; XPS, X-ray photoelectron spectroscopy; DFT, density functional theory

# REFERENCES

- (1) Ye, X.; He, X.; Lei, Y.; Tang, J.; Yu, Y.; Shi, H.; Wang, K. One-pot synthesized Cu/Au/Pt trimetallic nanoparticles with enhanced catalytic and plasmonic properties as a universal platform for biosensing and cancer theranostics. *Chem. Commun.* **2019**, *55*, 2321–2324.
- (2) Xu, C.; Yuan, Z.; Kohler, N.; Kim, J.; Chung, M. A.; Sun, S. FePt nanoparticles as an Fe reservoir for controlled Fe release and tumor inhibition. *J. Am. Chem. Soc.* **2009**, *131*, 15346–15351.
- (3) Lacey, S. D.; Dong, Q.; Huang, Z.; Luo, J.; Xie, H.; Lin, Z.; Kirsch, D. J.; Vattipalli, V.; Povinelli, C.; Fan, W.; Shahbazian-Yassar, R.; Wang, D.; Hu, L. Stable Multimetallic Nanoparticles for Oxygen Electrocatalysis. *Nano Lett.* **2019**, *19*, 5149–5158.
- (4) Park, J. H.; Ahn, H. S. Electrochemical synthesis of multimetallic nanoparticles and their application in alkaline oxygen reduction catalysis. *Appl. Surf. Sci.* **2020**, *504*, 144517.
- (5) Jo, C.; Kim, Y.; Hwang, J.; Shim, J.; Chun, J.; Lee, J. Block copolymer directed ordered mesostructured TiNb2O7 multimetallic oxide constructed of nanocrystals as high power Li-ion battery anodes. *Chem. Mater.* **2014**, *26*, 3508–3514.
- (6) Wang, Y.; Li, L.; Zhang, Y.; Chen, X.; Fang, S.; Li, G. Growth kinetics, cation occupancy, and magnetic properties of multimetal oxide nanoparticles: a case study on spinel NiFe2O4. *J. Phys. Chem. C* **2017**, *121*, 19467–19477.
- (7) Gao, S.; Hao, S.; Huang, Z.; Yuan, Y.; Han, S.; Lei, L.; Zhang, X.; Shahbazian-Yassar, R.; Lu, J. Synthesis of high-entropy alloy nanoparticles on supports by the fast moving bed pyrolysis. *Nat. Commun.* **2020**, *11*, 2016.
- (8) Zeng, Z.; Zhao, J.; Zhou, X.; Li, J.; Liang, B. Thermal stability of Al-Cu-Fe-Cr-Ni high entropy alloy bulk and nanoparticle structure: A molecular dynamics perspective. *Chem. Phys.* **2019**, *517*, 126–130.
- (9) Zhang, Y.; Tunes, M. A.; Crespillo, M. L.; Zhang, F.; Boldman, W. L.; Rack, P. D.; Jiang, L.; Xu, C.; Greaves, G.; Donnelly, S. E.; Wang, L.; Weber, W. J. Thermal stability and irradiation response of nanocrystalline CoCrCuFeNi high-entropy alloy. *Nanotechnology* **2019**, *30*, 294004.
- (10) Jin, X.; Gu, X.; Quan, F.; Ran, X.; Zhang, K.; Mao, A. CoCrFeMnNi high-entropy alloy powder with excellent corrosion resistance and soft magnetic property prepared by gas atomization method. *Materialwiss. Werkstofftech.* **2019**, *50*, 837–843.

- (11) Yang, X.; Zhou, Y.; Zhu, R.; Xi, S.; He, C.; Wu, H.; Gao, Y. A Novel, Amorphous, Non-equiatomic FeCrAlCuNiSi High-Entropy Alloy with Exceptional Corrosion Resistance and Mechanical Properties. *Acta Metall. Sin. (Engl. Lett.)* **2020**, *33*, 1057.
- (12) Vrtnik, S.; Guo, S.; Sheikh, S.; Jelen, A.; Koželj, P.; Luzar, J.; Kocjan, A.; Jagličić, Z.; Meden, A.; Guim, H.; Kim, H. J.; Dolinšek, J. Magnetism of CoCrFeNiZrx eutectic high-entropy alloys. *Intermetallics* 2018, 93, 122–133.
- (13) Zhang, Y.; Zuo, T. T.; Tang, Z.; Gao, M. C.; Dahmen, K. A.; Liaw, P. K.; Lu, Z. P. Microstructures and properties of high-entropy alloys. *Prog. Mater. Sci.* **2014**, *61*, 1–93.
- (14) Singh, M. P.; Srivastava, C. Synthesis and electron microscopy of high entropy alloy nanoparticles. *Mater. Lett.* **2015**, *160*, 419–422.
- (15) Stankic, S.; Suman, S.; Haque, F.; Vidic, J. Pure and multi metal oxide nanoparticles: synthesis, antibacterial and cytotoxic properties. *J. Nanobiotechnol.* **2016**, *14*, 73.
- (16) Osgood, H.; Devaguptapu, S. V.; Xu, H.; Cho, J.; Wu, G. Transition metal (Fe, Co, Ni, and Mn) oxides for oxygen reduction and evolution bifunctional catalysts in alkaline media. *Nano Today* **2016**, *11*, 601–625.
- (17) Wu, M.-L.; Chen, D.-H.; Huang, T.-C. Preparation of Au/Pt bimetallic nanoparticles in water-in-oil microemulsions. *Chem. Mater.* **2001**, *13*, 599–606.
- (18) Shen, H.; Gracia-Espino, E.; Wang, L.; Qin, D.; Gao, S.; Mamat, X.; Ren, W.; Wagberg, T.; Hu, G. Microwave-assisted synthesis of multimetal oxygen-evolving catalysts. *Electrochem. Commun.* **2017**, *81*, 116–119.
- (19) Zhang, N.; Feng, Y.; Zhu, X.; Guo, S.; Guo, J.; Huang, X. Superior bifunctional liquid fuel oxidation and oxygen reduction electrocatalysis enabled by PtNiPd core—shell nanowires. *Adv. Mater.* **2017**, *29*, 1603774.
- (20) Yang, S.; Guo, F.; Kiraly, B.; Mao, X.; Lu, M.; Leong, K. W.; Huang, T. J. Microfluidic synthesis of multifunctional Janus particles for biomedical applications. *Lab Chip* **2012**, *12*, 2097–2102.
- (21) Yao, Y.; Huang, Z.; Xie, P.; Lacey, S. D.; Jacob, R. J.; Xie, H.; Chen, F.; Nie, A.; Pu, T.; Rehwoldt, M.; Yu, D.; Zachariah, M. R.; Wang, C.; Shahbazian-Yassar, R.; Li, J.; Hu, L. Carbothermal shock synthesis of high-entropy-alloy nanoparticles. *Science* **2018**, 359, 1489–1494.
- (22) Yang, Y.; Song, B.; Ke, X.; Xu, F.; Bozhilov, K. N.; Hu, L.; Shahbazian-Yassar, R.; Zachariah, M. R. Aerosol synthesis of high entropy alloy nanoparticles. *Langmuir* **2020**, *36*, 1985–1992.
- (23) Siriwong, C.; Phanichphant, S. Flame-made single phase Zn2TiO4 nanoparticles. *Mater. Lett.* **2011**, *65*, 2007–2009.
- (24) Kammler, H. K.; Mädler, L.; Pratsinis, S. E. Flame synthesis of nanoparticles. *Chem. Eng. Technol.* **2001**, *24*, 583–596.
- (25) Goldstein, A.; Goldenberg, A.; Yeshurun, Y.; Hefetz, M. Transparent MgAl2O4 spinel from a powder prepared by flame spray pyrolysis. *J. Am. Chem. Soc.* **2008**, *91*, 4141–4144.
- (26) Savva, A.; Papadas, I. T.; Tsikritzis, D.; Ioakeimidis, A.; Galatopoulos, F.; Kapnisis, K.; Fuhrer, R.; Hartmeier, B.; Oszajca, M. F.; Luechinger, N. A.; Kennou, S.; Armatas, G. S.; Choulis, S. A. Inverted Perovskite Photovoltaics Using Flame Spray Pyrolysis Solution Based CuAlO2/Cu—O Hole-Selective Contact. ACS Appl. Energy Mater. 2019, 2, 2276—2287.
- (27) Ajayi, B. P.; Kumari, S.; Jaramillo-Cabanzo, D.; Spurgeon, J.; Jasinski, J.; Sunkara, M. A rapid and scalable method for making mixed metal oxide alloys for enabling accelerated materials discovery. *J. Mater. Res.* **2016**, *31*, 1596–1607.
- (28) Patey, T. J.; Ng, S. H.; Büchel, R.; Tran, N.; Krumeich, F.; Wang, J.; Liu, H. K.; Novák, P. Electrochemistry of LiV3O8 nanoparticles made by flame spray pyrolysis. *Electrochem. Solid-State Lett.* 2008, 11, A46.
- (29) Rudin, T.; Wegner, K.; Pratsinis, S. E. Uniform nanoparticles by flame-assisted spray pyrolysis (FASP) of low cost precursors. *J. Nanopart. Res.* **2011**, *13*, 2715–2725.
- (30) Punginsang, M.; Wisitsoraat, A.; Tuantranont, A.; Phanichphant, S.; Liewhiran, C. Ultrafine Bi2WO6 nanoparticles

- prepared by flame spray pyrolysis for selective acetone gas-sensing. *Mater. Sci. Semicond. Process.* **2019**, 90, 263–275.
- (31) Nagase, T.; Rack, P. D.; Noh, J. H.; Egami, T. In-situ TEM observation of structural changes in nano-crystalline CoCrCuFeNi multicomponent high-entropy alloy (HEA) under fast electron irradiation by high voltage electron microscopy (HVEM). *Intermetallics* **2015**, *59*, 32–42.
- (32) Zhang, P.; Lu, H.; Zhou, Y.; Zhang, L.; Wu, Z.; Yang, S.; Shi, H.; Zhu, Q.; Chen, Y.; Dai, S. Mesoporous MnCeO x solid solutions for low temperature and selective oxidation of hydrocarbons. *Nat. Commun.* 2015, 6, 8446.
- (33) Jiang, J.; Li, Y.; Liu, J.; Huang, X.; Yuan, C.; Lou, X. W. D. Recent advances in metal oxide-based electrode architecture design for electrochemical energy storage. *Adv. Mater.* **2012**, *24*, 5166–5180.
- (34) Arandiyan, H. R.; Parvari, M. Studies on mixed metal oxides solid solutions as heterogeneous catalysts. *Braz. J. Chem. Eng.* **2009**, 26, 63–74.
- (35) Hofmeister, H.; Huisken, F.; Kohn, B.; Alexandrescu, R.; Cojocaru, S.; Crunteanu, A.; Morjan, I.; Diamandescu, L. Filamentary iron nanostructures from laser-induced pyrolysis of iron pentacarbonyl and ethylene mixtures. *Appl. Phys. A* **2001**, *72*, 7–11.
- (36) Li, X.; Tan, G.; Chen, W.; Zhou, B.; Xue, D.; Peng, Y.; Li, F.; Mellors, N. J. Nanostructural and magnetic studies of virtually monodispersed NiFe 2 O 4 nanocrystals synthesized by a liquid–solid-solution assisted hydrothermal route. *J. Nanopart. Res.* **2012**, *14*, 751.
- (37) Yeh, J.-W.; Chang, S.-Y.; Hong, Y.-D.; Chen, S.-K.; Lin, S.-J. Anomalous decrease in X-ray diffraction intensities of Cu-Ni-Al-Co-Cr-Fe-Si alloy systems with multi-principal elements. *Mater. Chem. Phys.* **2007**, *103*, 41–46.
- (38) Holder, C. F.; Schaak, R. E. Tutorial on powder X-ray diffraction for characterizing nanoscale materials. *ACS Nano* **2019**, *13*, 7359–7365.
- (39) Yeh, J.-W.; Chen, S.-K.; Lin, S.-J.; Gan, J.-Y.; Chin, T.-S.; Shun, T.-T.; Tsau, C.-H.; Chang, S.-Y. Nanostructured high-entropy alloys with multiple principal elements: novel alloy design concepts and outcomes. *Adv. Eng. Mater.* **2004**, *6*, 299–303.
- (40) Zhang, F.; Tong, Y.; Jin, K.; Bei, H.; Weber, W.; Zhang, Y. Lattice distortion and phase stability of Pd-Doped NiCoFeCr solid-solution alloys. *Entropy* **2018**, *20*, 900.
- (41) Kalinowski, L.; Goraus, J.; Ślebarski, A. "DistorX" program for analysis of structural distortions affecting X-ray diffraction patterns. *AIP Adv.* **2018**, *8*, 101334.
- (42) Ślebarski, A.; Goraus, J.; Witas, P. Electrical resistivity of the heavy-fermion-filled cage compound Ce 3 M 4 Sn 13 (M= Co, Rh, Ru) under high pressure. *Phys. Rev. B: Condens. Matter Mater. Phys.* **2015**, *92*, 155136.
- (43) D'Ippolito, V.; Andreozzi, G. B.; Bersani, D.; Lottici, P. P. Raman fingerprint of chromate, aluminate and ferrite spinels. *J. Raman Spectrosc.* **2015**, *46*, 1255–1264.
- (44) Malavasi, L.; Galinetto, P.; Mozzati, M. C.; Azzoni, C. B.; Flor, G. Raman spectroscopy of AMn 2 O 4 (A= Mn, Mg and Zn) spinels. *Phys. Chem. Chem. Phys.* **2002**, *4*, 3876–3880.
- (45) Prins, R. Location of the Spinel Vacancies in  $\gamma$ -Al2O3. Angew. Chem., Int. Ed. 2019, 58, 15548–15552.
- (46) Tholkappiyan, R.; Naveen, A. N.; Vishista, K.; Hamed, F. Investigation on the electrochemical performance of hausmannite Mn3O4 nanoparticles by ultrasonic irradiation assisted co-precipitation method for supercapacitor electrodes. *J. Taibah Univ. Sci.* **2018**, *12*, 669–677.
- (47) Ramírez, A.; Hillebrand, P.; Stellmach, D.; May, M. M.; Bogdanoff, P.; Fiechter, S. Evaluation of MnO x, Mn2O3, and Mn3O4 electrodeposited films for the oxygen evolution reaction of water. *J. Phys. Chem. C* **2014**, *118*, 14073–14081.
- (48) Ai, Q.; Yuan, Z.; Huang, R.; Yang, C.; Jiang, G.; Xiong, J.; Huang, Z.; Yuan, S. One-pot co-precipitation synthesis of Fe 3 O 4 nanoparticles embedded in 3D carbonaceous matrix as anode for lithium ion batteries. *J. Mater. Sci.* **2019**, *54*, 4212–4224.

- (49) Yamashita, T.; Hayes, P. Analysis of XPS spectra of Fe2+ and Fe3+ ions in oxide materials. *Appl. Surf. Sci.* **2008**, 254, 2441–2449.
- (50) Wang, D.; Liu, Z.; Du, S.; Zhang, Y.; Li, H.; Xiao, Z.; Chen, W.; Chen, R.; Wang, Y.; Zou, Y.; Wang, S. Low-temperature synthesis of small-sized high-entropy oxides for water oxidation. *J. Mater. Chem. A* **2019**, *7*, 24211–24216.
- (51) Fujiwara, M.; Matsushita, T.; Ikeda, S. X-ray photoelectron spectroscopy of copper (II) complexes with donor sets of O4, N2O4, N2O2, N4, N2S2, and S4. *Anal. Sci.* **1993**, *9*, 289–291.
- (52) Dai, P.; Shen, X.; Lin, Z.; Feng, Z.; Xu, H.; Zhan, J. Band-gap tunable (Cu2Sn) x/3 Zn 1- x S nanoparticles for solar cells. *Chem. Commun.* **2010**, *46*, 5749–5751.
- (53) Xu, X.; Guo, Y.; Bloom, B. P.; Wei, J.; Li, H.; Li, H.; Du, Y.; Zeng, Z.; Li, L.; Waldeck, D. H. Elemental Core Level Shift in High Entropy Alloy Nanoparticles via X-ray Photoelectron Spectroscopy Analysis and First-Principles Calculation. *ACS Nano* 2020, 14, 17704–17712.
- (54) Sarkar, A.; Wang, Q.; Schiele, A.; Chellali, M. R.; Bhattacharya, S. S.; Wang, D.; Brezesinski, T.; Hahn, H.; Velasco, L.; Breitung, B. High-entropy oxides: fundamental aspects and electrochemical properties. *Adv. Mater.* **2019**, *31*, 1806236.
- (55) Murty, B. S.; Yeh, J.-W.; Ranganathan, S.; Bhattacharjee, P. High-Entropy Alloys; Elsevier, 2019; p 18.
- (56) Zhou, N.; Jiang, S.; Huang, T.; Qin, M.; Hu, T.; Luo, J. Single-phase high-entropy intermetallic compounds (HEICs): bridging high-entropy alloys and ceramics. *Sci. Bull.* **2019**, *64*, 856–864.
- (57) Heine, M. C.; Mädler, L.; Jossen, R.; Pratsinis, S. E. Direct measurement of entrainment during nanoparticle synthesis in spray flames. *Combust. Flame* **2006**, *144*, 809–820.
- (58) Teoh, W. Y.; Amal, R.; Mädler, L. Flame spray pyrolysis: An enabling technology for nanoparticles design and fabrication. *Nanoscale* **2010**, *2*, 1324–1347.
- (59) Skenderović, I.; Kotalczyk, G.; Kruis, F. E. Dual population balance Monte Carlo simulation of particle synthesis by flame spray pyrolysis. *Processes* **2018**, *6*, 253.
- (60) Meierhofer, F.; Mädler, L.; Fritsching, U. Nanoparticle evolution in flame spray pyrolysis—Process design via experimental and computational analysis. *AIChE J.* **2020**, *66*, No. e16885.
- (61) Koirala, R.; Pratsinis, S. E.; Baiker, A. Synthesis of catalytic materials in flames: opportunities and challenges. *Chem. Soc. Rev.* **2016**, *45*, 3053–3068.
- (62) Athanassiou, E. K.; Grass, R. N.; Stark, W. J. Chemical aerosol engineering as a novel tool for material science: from oxides to salt and metal nanoparticles. *Aerosol Sci. Technol.* **2010**, *44*, 161–172.
- (63) Bolsaitis, P. P.; McCarthy, J. F.; Mohiuddin, G.; Elliott, J. F. Formation of metal oxide aerosols for conditions of high supersaturation. *Aerosol Sci. Technol.* **1987**, *6*, 225–246.
- (64) Eslamian, M.; Shekarriz, M. Recent advances in nanoparticle preparation by spray and microemulsion methods. *Recent Pat. Nanotechnol.* **2009**, *3*, 99–115.
- (65) Abram, C.; Mezhericher, M.; Beyrau, F.; Stone, H. A.; Ju, Y. Flame synthesis of nanophosphors using sub-micron aerosols. *Proc. Combust. Inst.* **2019**, *37*, 1231–1239.